17. K. V. Hodges, *Annu. Rev. Earth Planet. Sci.* **19**, 207 (1991).
18. E. Herren, *Geology* **15**, 409 (1987).
19. A. Pêcher, *Tectonics* **10**, 587 (1991).
20. K. V. Hodges and L. W. McKenna, *Am. Mineral.* **72**, 671 (1987).
21. For information concerning analytical techniques, see Hodges and McKenna (*20*). We adopted the calibration of Hodges and McKenna for the garnet-biotite thermometer and that of L. W. McKenna and K. V. Hodges [*ibid.* **73**, 1205 (1988)] for the garnet-plagioclase-sillimanite-quartz barometer. Nonideal solution behavior was modeled for garnet [R. G. Berman, *ibid.* **75**, 328 (1990)] and for plagioclase (L. T. Elkins and T. L. Grove, *ibid.*, p. 544).
22. F. S. Spear and F. Florence, *J. Metamorph. Geol.* **9**, 379 (1991).
23. Analyses were done with the use of a VG Sector 54 mass spectrometer (Fisons Instruments, Danvers, MA) in static multicollector mode. The titanite was dissolved in a mixture of 0.5 ml of 6 N HCl and 0.1 ml of HF at 450 K (~175°C). Pb and U were separated with the use of HBr media and HNO_3-media anion exchange chemistry, respectively. Pb was loaded with silica gel and H_3PO_4 on

a Re filament, whereas U was loaded on Re with the use of H_3PO_4 and colloidal graphite and run as a metal
24. J. M. Mattinson, *Contrib. Mineral. Petrol.* **67**, 233 (1978).
25. M. Gascoyne, *Appl. Geochem* **1**, 199 (1986).
26. E. D. Ghent, M. Z. Stout, R. R. Parrish, in *Short Course on Heat, Metamorphism, and Tectonics*, E. G. Nisbet and C. M. R. Fowler, Eds. (Mineralogical Association of Canada, St. John's, 1988), vol. 14, pp. 155–188.
27. K. Mezger, C. M. Rawnsley, S. R. Bohlen, G. N. Hanson, *J. Geol.* **99**, 415 (1991).
28. For a description of $^{40}Ar/^{39}Ar$ analytical techniques at the University of Maine, see D. R. Lux [*Can. J. Earth Sci.* **23**, 21 (1986)]. Complete data tables for the R111 and R112 hornblendes are available on request.
29. P. Copeland, R. R. Parrish, T. M. Harrison, *Nature* **333**, 760 (1988).
30. U. Schärer, *Earth Planet. Sci Lett.* **67**, 191 (1984).
31. A description of analytical procedures for this facility may be found in R. R. Parrish, J. C. Roddick, W. D. Loveridge, R. W. Sullivan, in *Radiogenic Age and Isotopic Studies: Report 1* (Paper 87-2, Geological Survey of Canada, Otta-

wa, 1987), pp. 3–7.
32. P. K Zeitler and C P. Chamberlain, *Tectonics* **10**, 729 (1991)
33. R. R. Parrish, K. V. Hodges, A. Macfarlane, in *7th Himalaya-Tibet-Karakoram Workshop Abstracts*, M. P. Searle and P. J. Treloar, Eds. (Oxford University, Oxford, 1992), pp 67–68.
34. C. Ruppel, L. Royden, K. V. Hodges, *Tectonics* **7**, 947 (1988).
35. B. S. Hemingway, R. A. Robie, H. T. Evans, D. M. Kerrick, *Am. Mineral.* **76**, 1597 (1991).
36. A. B. Thompson, *Am. J. Sci.* **282**, 1567 (1982).
37. J. D. Clemens and V. J. Wall, *Can. Mineral.* **19**, 111 (1981).
38. D. Vielzeuf and J. R Holloway, *Contrib. Mineral. Petrol.* **98**, 257 (1988).
39 J. S. Stacey and J. D. Kramers, *Earth Planet. Sci. Lett.* **26**, 207 (1975).

The Seismic Attenuation Structure of a Fast-Spreading Mid-Ocean Ridge

William S. D. Wilcock,* Sean C. Solomon,† G. M. Purdy, Douglas R. Toomey

The two-dimensional P-wave attenuation structure of the axial crust of the East Pacific Rise was obtained from an inversion of waveform spectra collected during an active-source seismic tomography experiment. The structure shows that attenuation near the surface is high everywhere but decreases markedly within 1 to 3 kilometers of the rise axis. The near-axis variation is attributed to the thickening of the surface basalt layer and possibly to in situ changes in porosity related to hydrothermal circulation. High attenuation is also observed beneath the rise axis at depths ranging from about 2 kilometers (less than 1 kilometer beneath the axial magma lens) to the base of the crust. The levels of attenuation in this deeper region require at most only a small fraction of partial melt.

Mid-ocean ridges dominate the Earth's global volcanic flux and have been the locus of formation of the crust covering two-thirds of the Earth's surface. Models of the generation and early evolution of oceanic crust must be constrained by observations of the structure and physical state of crustal material near mid-ocean ridge axes. Because seismic-wave propagation is affected by the composition, tem-

perature, and porosity of the medium and by the presence of molten material, measurements of seismic properties are an important source of such constraints. Therefore, numerous experiments have measured the seismic velocity structure of mid-ocean ridges by such techniques as seismic refraction (*1*), multichannel reflection (*2, 3*) and expanding-spread (*4, 5*) profiling, and two- and three-dimensional (2-D and 3-D) tomography (*6–8*). A striking feature of the axial structure of fast-spreading ridges is a strong seismic reflector, at depths of 1 to 2 km, which has been interpreted as the roof of a thin magma lens or sill (*2, 9*). This feature is underlain by an extensive region of anomalously low velocities (*4–7*) that appears to extend to the base of the crust. In contrast, near-surface velocities on axis are markedly higher than elsewhere (*4–7, 10, 11*). One interpretation of the low-velocity region underlying the magma lens (*12*) is that it is a crystal mush zone extending downward to mid-crustal depths.

W. S. D. Wilcock, Massachusetts Institute of Technology—Woods Hole Oceanographic Institution Joint Program in Oceanography, Cambridge, MA 02139.
S. C. Solomon, Department of Earth, Atmospheric, and Planetary Sciences, Massachusetts Institute of Technology, Cambridge, MA 02139.
G. M. Purdy, Department of Geology and Geophysics, Woods Hole Oceanographic Institution, Woods Hole, MA 02543.
D. R. Toomey, Department of Geological Sciences, University of Oregon, Eugene, OR 97403.

*Present address: Institute of Geophysics and Planetary Physics 0225, University of California at San Diego, La Jolla, CA 92093.
†Present address: Department of Terrestrial Magnetism, Carnegie Institution of Washington, Washington, DC 20015.

Few studies have addressed directly the attenuative properties of oceanic crust (*13, 14*), although measurements of attenuation provide complementary information on the state of crustal material. Spatial variations in the levels of seismic attenuation can exceed an order of magnitude, much larger than those observed for seismic velocities. Measurements of attenuation do carry large uncertainties. However, they are particularly sensitive to the characteristics of regions of high attenuation that result from high porosities or near-solidus temperatures. In this report, we derive a 2-D model of compressional-wave (P-wave) attenuation across the East Pacific Rise. Our results provide constraints on the evolution of shallow oceanic crust and on the volume of the axial region that contains a significant fraction of partial melt.

The data set for this study comes from an active seismic tomography experiment conducted at 9°30′N on the East Pacific Rise (Fig. 1). A total of 480 well-navigated explosive shots of uniform mass (54.5 kg), construction, and depth of detonation were recorded by 15 accurately located, ocean-bottom hydrophones and seismometers (*6*). The experiment configuration was designed to optimize the resolution of delay-time tomographic velocity models (*6*) within a 16 by 16 km area of crust centered on the rise axis. To obtain an accurate record of the source signature and to demonstrate its uniformity, we made several mid-water recordings of the explosive source. In addition, the instrument response has been carefully determined for all of the receivers (*15*).

Attenuation tomography relies on an inversion of measurements of the attenuation of waveforms t^* for the quality factor Q (a physical property whose reciprocal measures anelasticity) with the relation

$$t^* = \int_s \frac{1}{VQ}\, ds \qquad (1)$$

where V is the seismic velocity and the integral is along the wave path s. We used a spectral technique to estimate t^*. The power spectrum resulting from propagation through the Earth P_E is related to the power spectrum of the recorded waveform P by

$$P_E(f) = \frac{P(f)}{P_S(f)\, P_I(f)} \qquad (2)$$

where P_S and P_I are the power spectra of the source and the instrument response, respectively, and f is frequency. If it is assumed that the sole frequency-dependent compo-
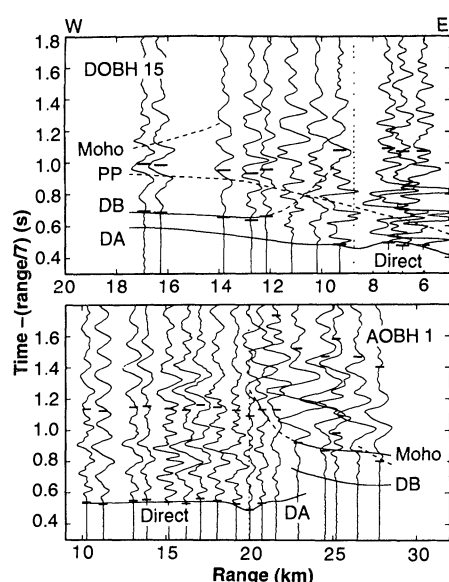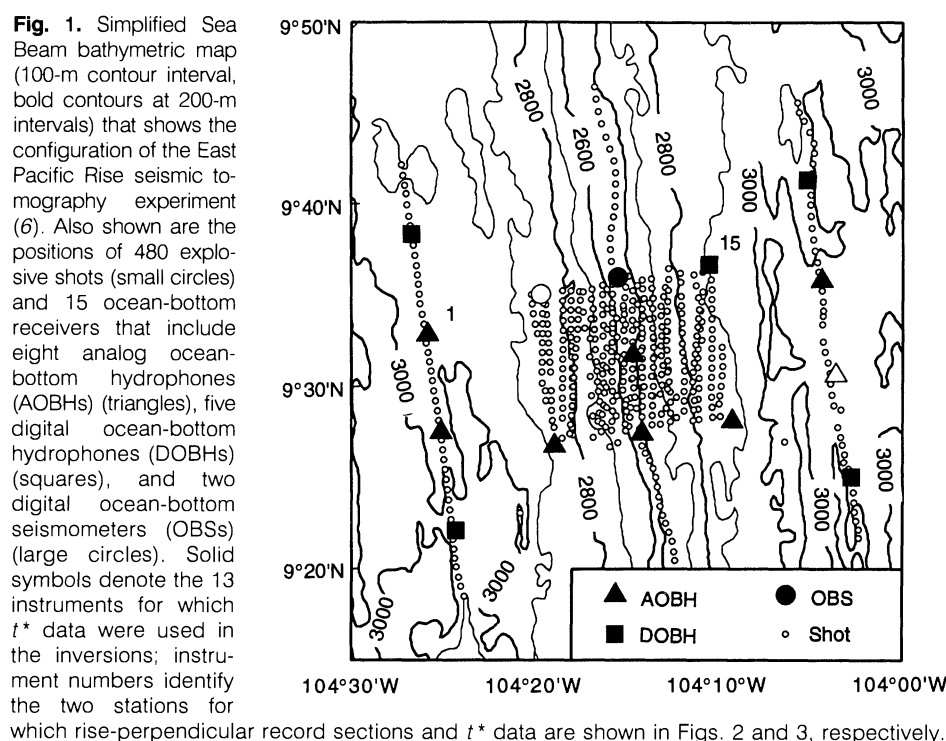
nent of seismic propagation is attenuation, then P_E will decrease exponentially with f according to

$$t^* = -\frac{1}{2\pi}\frac{d\ln[P_E(f)]}{df} \qquad (3)$$

We estimated P from a data window that was 0.3 or 0.6 s long (16), solved Eq. 2 for P_E, and estimated t^* according to Eq. 3 from a least-squares straight-line fit to a plot of $\ln(P_E)$ against frequency. This method also yields estimates of the relative uncertainties in t^* values.

In practice, the spectral estimates of t^* include contributions from frequency-dependent components of propagation other than

anelasticity such as scattering, focusing, multipathing, reverberations, and phase conversions, and so yield measures of apparent rather than intrinsic attenuation (17). The effects of multipathing can be minimized if one chooses a time window for the t^* estimate that is dominated by a single arrival. It is essential that the correct wave path be assigned to the t^* estimate. As an example, Fig. 2 shows rise-perpendicular record sections for two ocean-bottom hydrophones located 9 and 20 km off axis. The sections also show the time windows used for t^* estimates and the approximate arrival times of P phases identified by both full-waveform, finite-difference solutions (18) and ray tracing for a 2-D velocity model (5). For the receiver 9 km off axis (Fig. 2, top), the first arrival always passes above the magma chamber. However, at ranges greater than 11 or 12 km it is a diffracted phase whose amplitude decreases rapidly with

Fig. 1. Simplified Sea Beam bathymetric map (100-m contour interval, bold contours at 200-m intervals) that shows the configuration of the East Pacific Rise seismic tomography experiment (6). Also shown are the positions of 480 explosive shots (small circles) and 15 ocean-bottom receivers that include eight analog ocean-bottom hydrophones (AOBHs) (triangles), five digital ocean-bottom hydrophones (DOBHs) (squares), and two digital ocean-bottom seismometers (OBSs) (large circles). Solid symbols denote the 13 instruments for which t^* data were used in the inversions; instrument numbers identify the two stations for which rise-perpendicular record sections and t^* data are shown in Figs. 2 and 3, respectively.

Fig. 2. (Top) Record section for DOBH 15, located 9 km off axis (Fig. 1), for a profile oriented perpendicular to the rise. We applied a water-path correction (32) to ranges and travel times, scaled amplitudes linearly with range to correct for wave divergence, and applied a reduction velocity of 7 km/s to the data. Labeled solid lines show the approximate arrival times of phases identified with the aid of full-waveform, finite-difference solutions (18) and ray-theoretical wave paths, including a direct refracted crustal arrival and diffractions above (DA) and below (DB) the magma chamber. Dashed lines show the predicted times of additional arrivals that cannot be identified with certainty in the data. Horizontal ticks delimit the time windows used for spectral estimation of t^*, and the vertical dotted line shows the approximate location of the rise axis. **(Bottom)** As for (top) except that the record section is for AOBH 1, located 20 km off axis (Fig. 1).
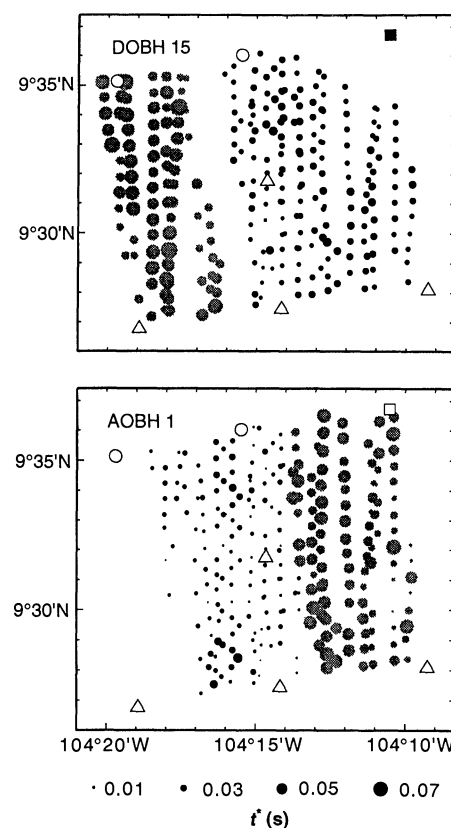
Fig. 3. (Top) Estimates of t^* for centrally located shots recorded by DOBH 15 (solid square). Values of t^* are plotted at the shot location as filled circles whose diameters increase linearly with t^*. Symbols for paths that do not cross the rise axis or that pass above the magma lens are in black and those for diffractions below the magma chamber are in gray. Instruments are indicated as in Fig. 1. **(Bottom)** Estimates of t^* for AOBH 1 (located to the west of the area shown) both for paths that do not cross the rise axis or that pass above the magma lens (black) and for Moho reflections (gray).

range, reaching values similar to those of the ambient noise. The first arrival with significant amplitude at such ranges is a diffraction below the magma chamber and is characterized by a marked decrease in high-frequency energy. Although no other P arrivals are clearly apparent at greater ranges, finite-difference models (18) suggest that both a high-amplitude PP phase, which includes a downward reflection off the sea floor near the rise axis and a reflection from the Moho, may be present. Therefore, a 0.6-s data window, which is long enough to include the full-source waveform, was used for

Fig. 4. Results of inversions for an axisymmetric, 2-D Q^{-1} model. (**A**) The 1-D starting model, derived from an inversion of data from rise-parallel paths located 20 km off axis. (**B**) The t^* data misfit (normalized to the nominal data uncertainties and the number of t^* observations) versus the smoothing weight μ (20). (**C**) A model of the apparent P-wave Q^{-1} structure for $\mu = 100$. Examples of the approximate wave paths illustrate the spatial sampling. (**D**) As for (C) except $\mu = 10$. (**E**) As for (C) except $\mu = 1$.

most estimates of t^*. However, a window 0.3 s long was used for the diffraction beneath the magma chamber to minimize possible contributions from later arrivals. For the receiver 20 km off axis (Fig. 2, bottom), the record section at ranges greater than ~22 km is dominated by a high-amplitude, low-frequency Moho reflection, arriving about 0.2 s after the diffraction below the magma chamber. Because this time interval is too short for us to obtain an unbiased estimate of t^* for the diffraction beneath the magma chamber, the t^* estimate was obtained for the Moho reflection with a window 0.6 s long.

The low frequencies of diffractions below the magma chamber and of the Moho reflections result in high t^* values for these phases (Fig. 3). Although the t^* estimates for waves that do not propagate across the rise axis are markedly lower, they are appreciably larger than zero and appear substantially independent of range, a characteristic that requires seismic attenuation off axis to be concentrated in the uppermost crust. The data also commonly show a significant decrease in t^* values for shots located near the rise axis.

The inversion of t^* data for Q^{-1} structures requires knowledge of both the velocity structure and the wave paths. We used the nodal velocity model obtained by travel time tomography (6) and extended it from depths of 5 to 8 km using a 2-D velocity model (5). Exact ray theory does not yield stable paths for many of the diffractions above and below the magma chamber, whereas the limited constraints on deeper velocity structure do not warrant the calculation of precise paths for the Moho reflection. We therefore used a modified version of the approximate ray-tracing algorithm used in the delay-time tomography (19). The resulting wave paths (Fig. 4, C to E) are generally good approximations of those deduced from ray theory and finite-difference calculations (18). For the phase diffracted beneath the magma chamber, the finite-difference solutions show that the wave is guided by the low-velocity region in and beneath the magma chamber. The waves propagate in this region between depths of 1.5 and 3 km before being strongly diffracted on the far side of the low-velocity region. We chose a depth beneath the rise axis of 2 to 2.5 km for this phase, a value that lies near the middle of the observed range of propagation depths in the finite-difference models and that is similar to that of an unstable exact ray path.
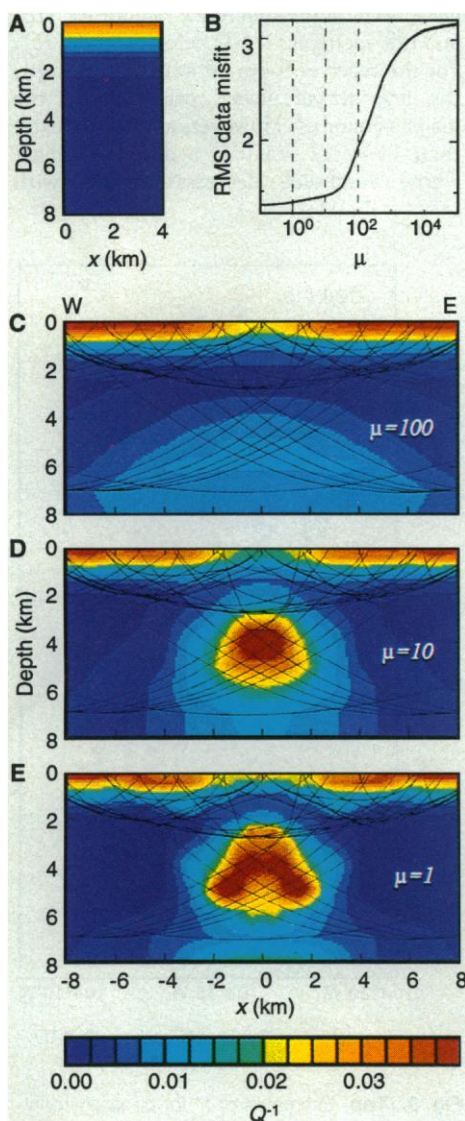
The t^* data set to be inverted comprises nearly 4000 waveforms recorded by 13 instruments. From the patterns in the data (Fig. 3), we chose to invert the observations for an axisymmetric, 2-D model. We calculated parameters for the attenuation

structure using linear interpolation between values at nodes spaced 0.5 to 1.0 km apart in a rectangular grid that was sheared vertically to conform with the sea floor. To ensure that the final model did not include physically unrealistic negative values for Q, the model was parameterized in terms of $\ln(Q^{-1})$, a procedure that sacrificed the linearity of Eq. 1. Constant t^* corrections for each receiver were also included in the inversion to account for local variations in structure beneath the receiver and for errors in the instrument responses. A smoothest model solution (20) was sought to the discrete version of Eq. 1.

The starting model (Fig. 4A) included average Q values of less than 50 in the uppermost 1 km and a constant Q of 500 below 3 km depth and was derived from a 1-D inversion of t^* estimates for shot-receiver pairs located 20 km off axis. Because the absolute uncertainties in t^* are not well known, an entirely objective choice of the smoothing weight μ, which reflects the relative importance of the model smoothness versus data misfit, cannot be made (Fig. 4B). The smoothest solution (Fig. 4C) lies at a point where the data misfit decreases rapidly with decreasing μ, whereas the data misfit for the roughest solution (Fig. 4E) is little changed from that of smoother solutions. The intermediate solution (Fig. 4D) might be considered preferable because it lies close to the point at which further reductions in μ no longer produce significant reductions in the data misfit. The variance reduction achieved by this solution is about 55% for all paths and nearly 75% for paths crossing the rise axis.

A marked feature common to all three solutions is the pronounced decrease in near-surface attenuation near the rise crest. In addition, the solutions show a region of low Q at depths greater than 2 km beneath the rise axis. This feature is not fully developed in the smoothest solution (Fig. 4C) because of the greater uncertainties associated with high t^* values. Complexities in the roughest solution (Fig. 4E) reflect the distribution of wave paths and are not well resolved because of the uncertainties associated with the velocity structure and wave paths in the lower crust.

Average Q values in the uppermost crust off axis are about 35, whereas the value on the axis doubles to about 70. In the inversion solutions, the anomalous region extends 2 to 3 km off axis, but, because smoothing broadens the anomaly, this width represents only an upper bound. The requirement that Q remain positive constrains the anomaly to extend at least 1 to 1.5 km off axis, a value in good agreement with the width of the axial high-velocity anomaly deduced from refraction experiments on the sea floor (11). Earlier workers

Fig. 5. Schematic cross section of the East Pacific Rise with a geological interpretation of the low-Q anomalies. The increase in near-surface attenuation off axis is attributed to an increase in the thickness of basalts and to the effects of hydrothermal circulation. A small upper crustal magma lens is required by other data (2, 5, 9) but is not imaged in the Q^{-1} inversions. This lens and any underlying region of high melt fraction or crystal mush (12) must be confined to the small area centered beneath the rise axis at 1 to 2 km depth that is devoid of wave paths (Fig. 4, C to E). An extensive low-Q region, whose precise shape is not well resolved, underlies the magma chamber and extends at least to the base of the crust. Here Q values are primarily the result of elevated temperatures, although the region may contain a small fraction of partial melt.
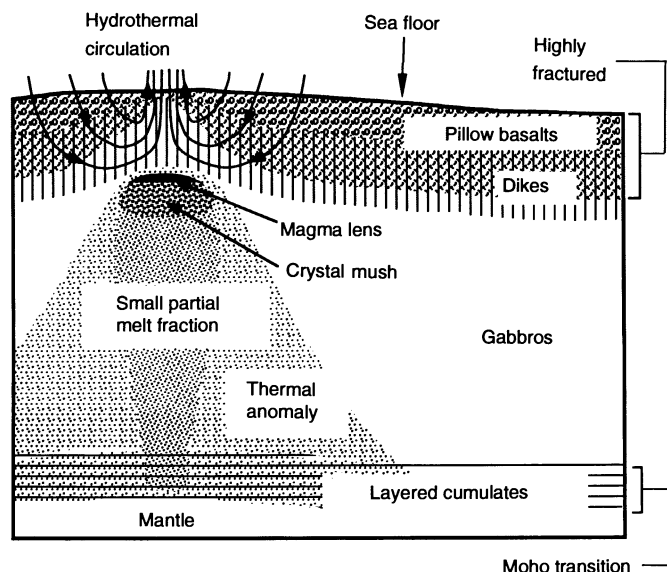
have suggested that the evolution in upper-crustal properties may result from either in situ changes in porosity that come from faulting (10) or from constructional thickening off axis of a basaltic layer with high porosity (6). Two observations support the second hypothesis. First, the narrow axial-summit graben observed in the area (21), coupled with models of mid-ocean ridge magmatism (22), suggests that the basalt layer is relatively thin at the rise axis (6). Second, the depth of a seismic reflector interpreted as the base of a surface basalt layer increases from between 100 and 200 m on axis to between 300 and 600 m off axis (11, 23, 24), whereas the thickness of underlying units remains constant (23). Thickening alone may not explain fully the change in attenuation, however, because Q values in the thickening layer would need to be 10 to 20, a range that is lower than near-surface values of 20 to 50 measured directly near the Juan de Fuca Ridge (13). Thus, in situ processes may also contribute to attenuation changes. Because large faults develop several kilometers off axis and show increased throws to distances of at least 20 km off axis at this location (25), faulting is unlikely to account for such rapid changes. It is more likely (Fig. 5) that increased attenuation in the upper 1 km off axis is related to high levels of hydrothermal circulation (21). Off axis, cool downflowing fluids induce cracking of host rocks and thus increase porosity (26), whereas hot fluids that ascend along the axis will heat the surrounding rocks and may reduce preexisting porosity both by thermal expansion (27) and by the rapid deposition of hydro-

thermal minerals (28). If there is also an increase off axis in the spatial variations in porosity on the scale of a seismic wavelength (~100 to 500 m), the observed increase in attenuation may include a contribution from scattering by velocity heterogeneities.

Although Q cannot be imaged in or immediately adjacent to the magma lens because of the absence of wave paths in this region, low axial Q values of 20 to 50 are resolved at depths ranging from ~2 km to the base of the crust. Such values presumably result from elevated temperatures and possibly the presence of partial melt associated with magmatic injection. Because Q may be strongly frequency-dependent, quantitative interpretation necessitates laboratory measurements not only at the appropriate compositions, temperatures, and pressures but also at seismic frequencies. Although no experiments to date fully satisfy these requirements, torsional oscillation measurements on basalts and gabbros (29) have been obtained at seismic frequencies, ambient pressure, and temperatures up to or just above the solidus. For a ratio of P-wave Q to S-wave Q of 2.25 (30), the results suggest that as temperature increases by several hundred degrees to the solidus, Q_P at 10 Hz decreases from 500 to 1000 to approximately 20 to 40 at the solidus. Because the latter range overlaps the lowest values imaged in the axial low-Q zone and Q can be expected to decrease further in the presence of partial melt (31), the laboratory data (29) suggest that the inversion results require at most only a few percent partial melt (Fig. 5). Because the diffrac-

tions below the magma chamber pass within 1 km of the roof of the magma lens (Fig. 4, C to E), the results constrain the magma chamber, shown schematically in Fig. 5 to include the magma lens and an underlying crystal mush zone (12), to have a thickness of less than 1 km. Therefore, models of oceanic crustal generation must account for the efficient delivery of melt through the lower crust to a small upper crustal magma chamber.

REFERENCES AND NOTES

1. J. A. Orcutt, B. L. N. Kennett, L. M. Dorman, *Geophys. J. R. Astron. Soc.* **45**, 305 (1976); G. M. Purdy and J. I. Ewing, in *The Geology of North America: The Western North Atlantic Region*, P. Vogt and B. Tucholke, Eds. (Geological Society of America, Boulder, CO, 1985), vol. M, pp. 303–330; G. M. Purdy and R. S. Detrick, *J. Geophys. Res.* **91**, 3739 (1986).
2. T. J. Herron, W. J. Ludwig, P. L. Stoffa, T. K. Kan, P. Buhl, *J. Geophys. Res.* **83**, 798 (1978); R. S. Detrick et al., *Nature* **326**, 35 (1987).
3. R. S. Detrick, J. C. Mutter, P. Buhl, I. I. Kim, *Nature* **347**, 61 (1990).
4. A. J. Harding et al., *J. Geophys. Res.* **94**, 12163 (1989).
5. E. E. Vera et al., *ibid.* **95**, 15529 (1990).
6. D. R. Toomey, G. M. Purdy, S. C. Solomon, W. S. D. Wilcock, *Nature* **347**, 639 (1990).
7. M. S. Burnett, D. W. Caress, J. A. Orcutt, *ibid.* **339**, 206 (1989); D. W. Caress, M. S. Burnett, J. A. Orcutt, *J. Geophys. Res.* **97**, 9243 (1992).
8. D. R. Toomey, S. C. Solomon, G. M. Purdy, *J. Geophys. Res.* **93**, 9093 (1988); L. S. L. Kong, S. C. Solomon, G. M. Purdy, *ibid.* **97**, 1659 (1992).
9. G. M. Kent, A. J. Harding, J. A. Orcutt, *Nature* **344**, 650 (1990).
10. J. S. McClain, J. A. Orcutt, M. Burnett, *J. Geophys. Res.* **90**, 8627 (1985).
11. G. L. Christeson, G. M. Purdy, G. J. Fryer, *Geophys. Res. Lett.* **19**, 1045 (1992).
12. J. M. Sinton and R. S. Detrick, *J. Geophys. Res.* **97**, 197 (1992).
13. R. S. Jacobson and B. T. R. Lewis, *ibid.* **95**, 17417 (1990).
14. W. W. Wepfer and N. I. Christensen, *ibid.*, p. 17430; *Mar. Geophys. Res.* **13**, 227 (1991).
15. A. M. Tréhu, thesis, Massachusetts Institute of Technology–Woods Hole Oceanographic Institution (MIT–WHOI) Joint Program (MIT–WHOI); W. S. D. Wilcock, thesis, MIT–WHOI Joint Program (1992).
16. The power spectrum *P* is calculated by multiple-window spectral analysis [D. J. Thomson, *Proc. IEEE* **70**, 1055 (1982); J. Park, C. R. Lindberg, F. L. Vernon III, *J. Geophys. Res.* **92**, 12675 (1987)] with 4-π prolate tapers. P_E is calculated from Eq. 2 after P_S and P_I have been smoothed to account for the frequency resolution of the spectral estimator. Synthetic tests show that if at least 0.3 s of data is used, the limited frequency resolution of the spectral estimate does not bias the estimates of t^* by more than ~5%. Moreover, estimates satisfying this criterion are not very sensitive to the uncertainties in the source spectrum.
17. V. F. Cormier, *Bull. Seismol. Soc. Am.* **72**, S169 (1982).
18. M. E. Dougherty, W. S. D. Wilcock, S. C. Solomon, *Eos* **72** (fall suppl.), 309 (1991); W. S. D. Wilcock, M. E. Dougherty, S. C. Solomon, D. R. Toomey, G. M. Purdy, *ibid.*, p. 495.
19. The approximate pseudo-bending, ray-tracing algorithm [J. Um and C. Thurber, *Bull. Seismol. Soc. Am.* **77**, 972 (1987)] is used to search for a minimum time path of constant curvature and to distort iteratively this path toward a ray-theoretical path. To ensure that these paths closely approximate those of the desired phases, we limit the range of the initial search for a constant-curvature path. In addition, near-zero velocities are placed

1473

at strategic nodes beneath the rise axis so that paths pass to the correct side of the magma lens. Because the nodes of near-zero velocity strongly influence the placement of paths, the asymmetric displacement of the low-velocity zone to the west in the delay-time tomographic velocity model (6) and in multichannel reflection data [J. C. Mutter *et al., Nature* **336**, 156 (1988)] is not reflected in the approximate paths.

20. The smoothest model inversion algorithm [A. N. Tikhonov and V. Y. Arsenin, *Solutions of Ill-Posed Problems* (Wiley, New York, 1977); S. C. Constable, R. L. Parker, C. G. Constable, *Geophysics* **52**, 289 (1987)] minimizes the weighted sum of the misfit to the data and the roughness of the model measured with the use of first-order differences

$$(t_o - t_m)^T R_{tt}^{-1}(t_o - t_m) + \mu(q_a - q_m)^T \Delta^T \Delta(q_a - q_m)$$

where t_o is a vector of the t^* observations, t_m is the model predictions, R_{tt} is a diagonal matrix of the estimated data variances, μ is the weight of the smoothing constraint, q_a is the vector of the $\ln(Q^{-1})$ nodal values in the starting model, q_m is the current model, Δ is an operator that calculates the first-order differences between all adjacent nodes, and T denotes transpose.

21. R. M. Haymon *et al., Earth Planet. Sci. Lett.* **104**, 513 (1991).
22. J. R. Cann, *Geophys. J. R. Astron. Soc.* **39**, 169 (1974); R. G. W. Kidd, *ibid.* **51**, 149 (1977)
23. A. J. Harding, G. M. Kent, M. E Kappus, J A Orcutt, *Eos* **72** (fall suppl.), 494 (1991).
24. E. E. Vera and J. B. Diebold, *ibid.*, p 495.
25. W. S. D. Wilcock, D R Toomey, G. M. Purdy, S C Solomon, *Mar. Geophys. Res.*, in press.
26. C. R. B. Lister, *Geophys. J. R. Astron. Soc.* **39**, 465 (1974)
27. R. P. Lowell, *Geophys. Res. Lett* **17**, 709 (1990), L. N. Germanovich and R. P. Lowell, *Science* **255**, 1564 (1992).
28 J R. Delaney, D. W. Mogk, M. J. Mottl, *J. Geophys. Res.* **92**, 9175 (1987).
29. W. Kampfmann and H. Berckhemer, *Phys. Earth Planet. Inter.* **40**, 223 (1985).
30. D. L. Anderson, *Geophys. J. R. Astron. Soc.* **14**, 135 (1967).
31. G. Mavko and A. Nur, *J. Geophys. Res.* **80**, 1444 (1975).
32. G. M. Purdy, *ibid.* **87**, 8389 (1982).
33. We thank the officers and crew of the R.V. *Thomas Washington* and members of the scientific party for their assistance. Supported by the Office of Naval Research grant N00014-89-J-1257, the National Science Foundation grants OCE-8615797 and OCE-8615892 (for the original data collection), and WHOI Contribution 8150.
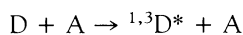
20 July 1992; accepted 24 September 1992

Photoinduced Electron Transfer from a Conducting Polymer to Buckminsterfullerene
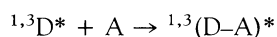
N. S. Sariciftci, L. Smilowitz, A. J. Heeger, F. Wudl

Evidence for photoinduced electron transfer from the excited state of a conducting polymer onto buckminsterfullerene, C_{60}, is reported. After photo-excitation of the conjugated polymer with light of energy greater than the π–π^* gap, an electron transfer to the C_{60} molecule is initiated. Photoinduced optical absorption studies demonstrate a different excitation spectrum for the composite as compared to the separate components, consistent with photo-excited charge transfer. A photoinduced electron spin resonance signal exhibits signatures of both the conducting polymer cation and the C_{60} anion. Because the photoluminescence in the conducting polymer is quenched by interaction with C_{60}, the data imply that charge transfer from the excited state occurs on a picosecond time scale. The charge-separated state in composite films is metastable at low temperatures.

Photoinduced electron transfer has been extensively investigated in physics, chemistry, and biology (and in the interdisciplinary areas of overlap between the traditional disciplines) because of fundamental interest in the photophysics and photochemistry of excited states in organic molecules and because such studies provide a synthetic approach to a deeper understanding of solar energy conversion in green plants (1). A basic description of intramolecular or intermolecular photoinduced electron transfer is as follows:
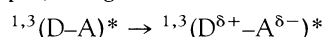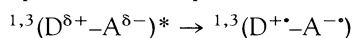
Step 1, excitation on D:

$$D + A \rightarrow {}^{1,3}D^* + A$$

Step 2, excitation delocalized on the D–A complex:

$${}^{1,3}D^* + A \rightarrow {}^{1,3}(D\text{–}A)^*$$

Institute for Polymers and Organic Solids, University of California, Santa Barbara, CA 93105.

Step 3, charge transfer initiated:

$${}^{1,3}(D\text{–}A)^* \rightarrow {}^{1,3}(D^{\delta+}\text{–}A^{\delta-})^*$$

Step 4, ion radical pair formed:

$${}^{1,3}(D^{\delta+}\text{–}A^{\delta-})^* \rightarrow {}^{1,3}(D^{+\cdot}\text{–}A^{-\cdot})$$

Step 5, charge separation:

$${}^{1,3}(D^{+\cdot}\text{–}A^{-\cdot}) \rightarrow D^{+\cdot} + A^{-\cdot}$$
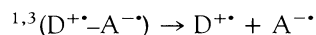
In these equations the donor (D) and acceptor (A) units are either covalently bonded (intramolecular) or spatially close but not covalently bonded (intermolecular); 1 and 3 denote singlet or triplet excited states, respectively. At each step, the D–A system can relax back to the ground state either by releasing energy to the "lattice" (in the form of heat) or by emitting light (provided the radiative transition is allowed). Permanent changes that may occur from ion radical reactions beyond step 5 are not considered here,

even though their importance in photochemical reactions has been established. The electron transfer (step 4) describes the formation of an ion radical pair; this does not occur unless $I_{D^*} - A_A - U_C < 0$, where I_{D^*} is the ionization potential of the excited state (D^*) of the donor, A_A is the electron affinity of the acceptor, and U_C is the Coulomb energy of the separated radicals (including polarization effects). The charge separation (step 5) can possibly be stabilized by carrier delocalization on the D^+ (or A^-) species and by structural relaxation.

The possibility of using such charge separation in molecular information storage and optoelectronics has been suggested (2). Donor-bridge-acceptor–type "supermolecules" have been proposed as bistable "molecular information storage units," in which the separated ion radical pair state is visualized as one logic state and the ground state is the second logic state (3). For intramolecular photoinduced electron transfer, the requirements on the spacer between the donor and acceptor units are important (and demanding); for metastability, the molecular orbitals of the D and A components must be decoupled so as to retard the back electron transfer process (4–6).

The discovery of conducting polymers and the ability to dope these polymers over the full range from insulator to metal have resulted in the creation of a class of new materials that combines the electronic and optical properties of semiconductors and metals with the attractive mechanical properties and processing advantages of polymers (7). Moreover, the ability to control the energy gap and electronegativity through molecular design has made possible the synthesis of conducting polymers with a range of ionization potentials and electron affinities (7–9). The extended π-orbitals of conjugated polymers result in a quasi–one-dimensional electronic structure with associated novel nonlinear excitations (solitons, polarons, bipolarons) (7–14). The unique combination of electronic, electrochemical, and mechanical properties of these synthetic metals and semiconductors plus the ability to expand the class of materials and control their properties through rational chemical synthesis have made conjugated polymers a promising field of interdisciplinary research.

As a new form of carbon, buckminsterfullerene, C_{60}, has generated considerable recent interest in the scientific community (15–17). This molecule is an excellent electron acceptor capable of taking on as many as six electrons (18, 19); C_{60}, therefore, forms charge transfer salts with a variety of strong donors. The discovery of important solid-state properties in such charge-transfer salts of C_{60} has opened